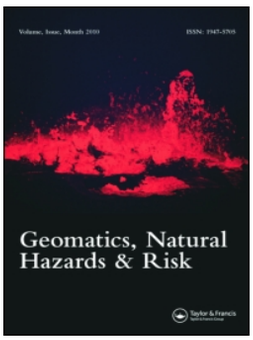

Geomatics, Natural Hazards and Risk

ISSN: 1947-5705 (Print) 1947-5713 (Online) Journal homepage: https://www.tandfonline.com/loi/tgnh20

Fast terrain modelling for hydrogeological risk mapping and emergency management: the contribution of high-resolution satellite SAR imagery

A. Nascetti, P. Capaldo, M. Porfiri, F. Pieralice, F. Fratarcangeli, L. Benenati & M. Crespi

To cite this article: A. Nascetti, P. Capaldo, M. Porfiri, F. Pieralice, F. Fratarcangeli, L. Benenati & M. Crespi (2015) Fast terrain modelling for hydrogeological risk mapping and emergency management: the contribution of high-resolution satellite SAR imagery, Geomatics, Natural Hazards and Risk, 6:5-7, 554-582, DOI: 10.1080/19475705.2014.904824

To link to this article: https://doi.org/10.1080/19475705.2014.904824

Published online: 14 Apr 2014.

Geomatics, Natural Hazards and Risk, 2015
Vol. 6, Nos. 5–7, 554–582, http://dx.doi.org/10.1080/19475705.2014.904824

Fast terrain modelling for hydrogeological risk mapping and emergency management: the contribution of high-resolution satellite SAR imagery

A. NASCETTI*, P. CAPALDO, M. PORFIRI, F. PIERALICE, F. FRATARCANGELI, L. BENENATI and M. CRESPI

DICEA, Geodesy and Geomatics Division, University of Rome "La Sapienza", 00184 Rome, Italy

(*Received 10 June 2013; accepted 11 March 2014*)

Geomatic tools fast terrain modelling play a relevant role in hydrogeological risk mapping and emergency management. Given their complete independence from logistic constraints on the ground (as for airborne data collection), illumination (daylight), and weather (clouds) conditions, synthetic aperture radar (SAR) satellite systems may provide important contributions in terms of digital surface models (DSMs) and digital elevation models (DEMs).

For this work we focused on the potential of high-resolution SAR satellite imagery for DSM generation using an interferometric (InSAR) technique and using a revitalized radargrammetric stereomapping approach. The goal of this work was just methodological. Our goal was to illustrate both the fundamental advantages and drawbacks of the radargrammetric approach with respect to the InSAR technique for DSM generation, and to outline their possible joint role in hydrogeological risk mapping and emergency management. Here, it is worth mentioning that radargrammetry procedures are independent of image coherence (unlike the interferometric approach) and phase unwrapping, as well as of parsimony (only a few images are necessary). Therefore, a short time is required for image collection (from tens of minutes to a few hours), thanks to the independence from illumination and weather. The most relevant obstacles of the technique are speckle and the lack of texture impact on image matching, as well as the well-known deformations of SAR imagery (layover and foreshortening), which may produce remarkable difficulties with complex morphologies and that must be accounted for during acquisition planning.

Here, we discuss results obtained with InSAR and radargrammetry applied to a COSMO-SkyMed SpotLight triplet (two stereopairs suited for radargrammetry and InSAR, sharing one common image) acquired over suburbs of San Francisco (United States), which are characterized by mixed morphology and land cover. We mainly focused on urban areas and zones covered by bare soil and rocks. Image processing was performed using the well-known commercial software SARscape® for InSAR, and the radargrammetric suite implemented in SISAR, software developed at the Geodesy and Geomatic Division of the University of Rome "La Sapienza".

Global accuracies were approximately 5 m using both approaches. However, several differences in terrain morphology reconstruction were determined and are underlined and evaluated here, as well as a possible way to further enhance the results using the integration of InSAR and radargrammetry.

*Corresponding author. Email: andrea.nascetti@uniroma1.it

1. Introduction

Landslides and flooding result in extensive damage to both property and lives. Therefore, hydrogeological and hydrological studies are essential both for town and country management and planning, and for environmental protection. Based on recent work, related to hydrogeological (Fell et al. 2008; Park & Chi 2008) and hydrological (Schumann et al. 2010; Yamazaki et al. 2011) risks, the importance of satellite remote sensing is becoming more and more recognized, because it offers an efficient way to obtain large-scale spatial information with both optical and synthetic aperture radar (SAR) sensors. Satellite imagery and derived secondary products play a fundamental role in supplying the information necessary for producing comprehensive landslide and flooding inventories, a must for quantifying hazards and vulnerable areas.

With regard to the hydrogeological risk, digital elevation models (DEMs) and digital surface models (DSMs) clearly play an important role, as outlined in a recent and very comprehensive review (van Westen et al.2008), which emphasizes their contribution to landslide hazard assessments on four mapping scales (small, medium, large, and detailed). With regard to the hydrological risk, secondary products also form a useful tool for refining flood inundation models and stream network identification, which is fundamental in mitigating the effects of flooding (Mason et al. 2011; Neal et al. 2012).

The goals of this work were just methodological. Here, we provide the actual potential of DSM generation from high-resolution satellite SAR imagery, and propose a comparison between the well-known interferometric (InSAR) technique and the less used but now revitalized and promising radargrammetric approach. The topic is not new (Gelautz et al. 2003; Sansosti 2004). However, it deserves renewed attention due to the availability of high-resolution SAR imagery collected by new satellite missions such as COSMO-SkyMed (Italian), TerraSAR-X (German), and RADARSAT-2 (Canadian).

In general, the fundamental advantage of these approaches is they involve working with only a pair of images, collected within a short period of time (a half day to a few days), thanks to the complete independence of satellite radar acquisition from logistics constraints on the ground (as for airborne data collection), illumination (daylight), and weather (clouds) conditions.

Until now, SAR imagery has mainly been employed for DSM generation using the InSAR approach. Special missions, such as the Shuttle Radar Topography Mission (SRTM), or more recently TanDEM-X (ongoing), have been designed and built to yield elevation data on a world scale. Over the last two decades, InSAR has developed from a theoretical concept into a technique that is being utilized at an increasing rate in a wide range of Earth science fields. At least a pair of images of the same area acquired from slightly different look angles (stereopair) are needed to perform the 3D reconstruction. This can be obtained either simultaneously using two radar antennas mounted on the same platform (single pass interferometry) or at different times by exploiting repeated orbits of the same satellite (repeat pass interferometry). The InSAR technique uses the phase difference between the signals backscattered by the terrain to retrieve height information and requires coherence between the images.

On the other hand, the radargrammetric approach deals with the amplitude of SAR imagery and does not require coherence between images. In particular,

radargrammetry was first employed in the 1950s with ground and airborne radars, and then its use became less and less practised with the passage of time, due to the low amplitude resolution of radar satellite imagery. The accuracy of radargrammetry directly depends on the spatial resolution of the SAR image, whereas InSAR accuracy depends on the signal wavelength, which is much smaller than the amplitude resolution and provides much higher accuracy. Only over the last few years, thanks to very high resolution imagery acquired using the previously mentioned new high-resolution satellite missions, it has been possible to supply images up to 1 m in ground sample distance (GSD). Given new missions, the radargrammetric approach has been revitalized and investigations have been restarted (Toutin & Chenier 2009; Capaldo et al. 2011; Perko et al. 2011). Analogous to optical photogrammetry, radargrammetry is based (at least) on a stereopair that must be acquired under a suited geometric configuration. As mentioned, only the amplitude information from SAR imagery is utilized. Grey values of each SAR image depend on several characteristics of the imaged surface, which reflect a certain amount of radiation according to geometrical and physical characteristics. As for photogrammetry, two values are required for DSM generation, stereopair orientation, and image matching for point cloud generation.

In the following, we discuss results obtained using InSAR and radargrammetry as applied to a COSMO-SkyMed SpotLight triplet (two stereopairs suited for radargrammetry and InSAR sharing a common image) specifically acquired over the suburbs of San Francisco (United States), which is characterized by mixed morphology and land cover. We largely focused on urban areas and zones covered by bare soil and rocks. Image processing was performed using the well-known commercial software SARscape® for InSAR, and the radargrammetric suite implemented in SISAR, scientific software developed at the Geodesy and Geomatic Division of the University of Rome "La Sapienza".

In Section 2, a short description of the images and the reference data are provided. Then, in Section 3, following the analytical framework introduced in Gelautz et al. (2003) and thoroughly developed in Sansosti (2004), we recall a common general model both for radargrammetry and for InSAR, pointing out the major critical problems of the two approaches in regard to DSM generation. Subsequently, in Sections 4 and 5, an analysis of the processing chains of the two approaches is carried out by customizing the common general model and focusing on the above-mentioned major critical problems. Finally, an accuracy assessment of the two DSM tiles using an extension of 2-3 km, performed using the software DEMANAL (developed by Dr K. Jacobsen at Leibniz University, Hannover, Germany) which allows a full 3D DSM comparison with the possible removal of horizontal bias, is done.

2. Dataset and reference DSM

Three SpotLight Cosmo-SkyMed images were acquired over the area of San Francisco, suitable for obtaining an interferometric pair and two radargrammetric stereopairs (table 1). Images for radargrammetry were chosen in order to obtain meaningful same side geometry. The interferometric pair was characterized by very similar view angles and a close time of acquisition (24 hours between the two acquisitions), suitable to guarantee good coherence crucial for interferometric processing.

Table 1. San Francisco images' main characteristics.

Used for interferometry	Master	Slave	–
Used for radargrammetry	Master	–	Slave
Acquisition date	8/2/2012	9/2/2012	14/2/2012
Acquisition mode	SpotLight Right	SpotLight Right	SpotLight Right
Satellite	CSK 2	CSK 3	CSK 2
Pass	Ascending	Ascending	Ascending
Acquisition start time	13:48:56	13:48:53	14:00:53
Acquisition end time	13:48:57	13:48:55	14:00:55
Width (km)	10.000	10.000	10.000
Length (km)	9.999	9.999	9.998
Swath area (km^2)	100.319	100.319	100.302
Near look angle (°)	19.887	19.827	37.376
Near incidence angle (°)	21.935	21.868	41.808
Range spacing (m)	0.702	0.702	0.702
Azimuth spacing (m)	0.314	0.314	0.372
Centre latitude	37.221	37.210	37.228
Centre longitude	−121.772	−121.770	−121.765

We additionally selected a location with favourable climatic and topographic conditions, slopes not too steep, sparse vegetation, and low atmospheric humidity. All of these factors, together with a good acquisition geometry, preserved phase coherence.

For the accuracy assessment, a Light Detection and Ranging (LiDAR) DSM was used as a reference. San Francisco LiDAR raw data (point cloud) are freely distributed by the United States Geological Survey (USGS) and have a horizontal and vertical accuracy of 0.75 m and 0.25 m, respectively, at 95% confidence level. Beginning from the orthometric height, the corresponding ellipsoidal heights were computed by adding geoidal undulation according to the USGS model GEOID03 adopted here. Then, the LiDAR DSM at ellipsoidal heights was resampled on a 1.5 m grid using bilinear interpolation.

The tiles used for the accuracy assessment are shown in figure 1. The right tile is characterized by morphological variety (hills, urban area). The left tile was chosen to highlight some of the problems related to interferometric processing.

3. Radargrammetry and InSAR: common model, different major problems

Radargrammetry and InSAR DSM generation are based on a common analytical model that can be easily customized for the two approaches and that is useful for easily highlighting their major problems, including image matching for radargrammetry and phase unwrapping for InSAR. This common model is based on zero-Doppler geometry: The target is acquired on a heading perpendicular to the flying direction of the satellite. Beginning with an image pair acquired from the two passages, the common model can be written in the form of the observation equations (1) of radar target acquisition (the slant range constraint) and zero-Doppler focalization in an Earth-Centered, Earth-Fixed (ECEF) coordinate system (usually the WGS84), using

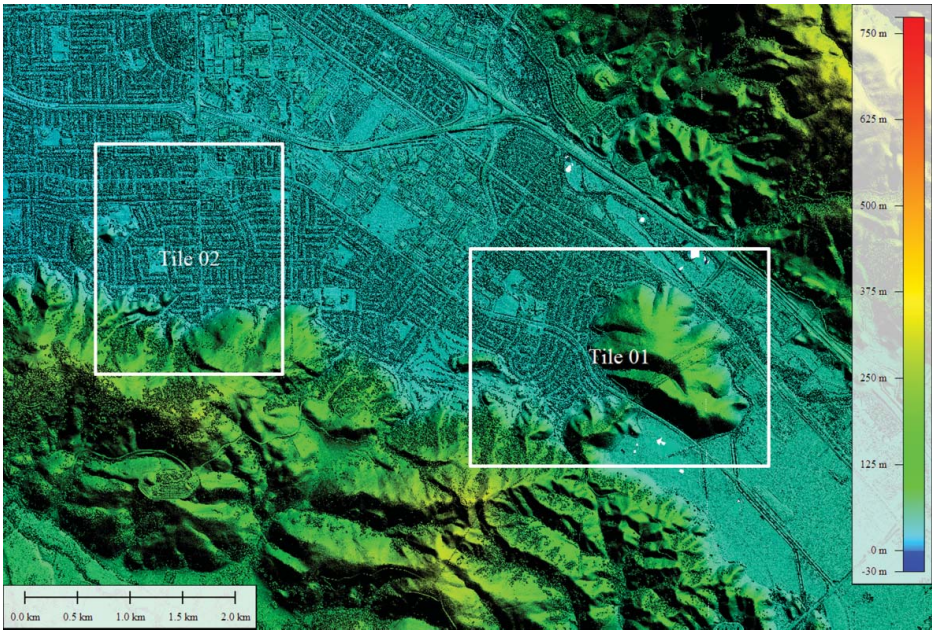

Figure 1. LiDAR DSM used for accuracy assessment and considered tiles.

the hypothesis of time-scale synchronization between the two passages (the time offset known or equal to zero) (figure 2), as follows:

$$\begin{cases} \rho_1(t_1) = |\mathbf{P} - \mathbf{S}_1(t_1)| \\ \mathbf{u}_1(t_1)\cdot(\mathbf{P} - \mathbf{S}_1(t_1) = 0 \\ \boldsymbol{\rho}_2(t_2) = |\mathbf{P} - \mathbf{S}_2(t_2)| \\ \mathbf{u}_2(t_2)\cdot(\mathbf{P} - \mathbf{S}_2(t_2)) = 0 \end{cases} \tag{1}$$

where $\mathbf{P}(X_P, Y_P, Z_P)$ is the generic ground point (GP) in the ECEF coordinate – unknown; $\mathbf{S}_i(t_i)(X_{S_i}(t_i), Y_{S_i}(t_i), Z_{S_i}(t_i))$ is the position of the sensor in the ith passage ($i = 1, 2$) at the epoch t_i – known from orbital information within the image metadata; $\rho_i(t_i)$ is the slant range between the sensor position $\mathbf{S}_i(t_i)$ and the point on the ground $\mathbf{P}$ at the epoch t_i – obtained through observation; and $\mathbf{u}_i(t_i)(u_{X_i}(t_i), u_{Y_i}(t_i), u_{Z_i}(t_i))$ is the unit velocity vector of the sensor in the ith passage ($i = 1, 2$) at the epoch t_i – known from orbit information within image metadata.

The mentioned radar rays can simply be modelled as two segments with measured lengths centred in two different positions (along two different satellite orbits) such that the intersection generating each object point is one of the two possible intersections between two circumferences centred in two different positions and lying in two planes orthogonal to two different satellite orbits whose radii are equal to the segment's measured lengths.

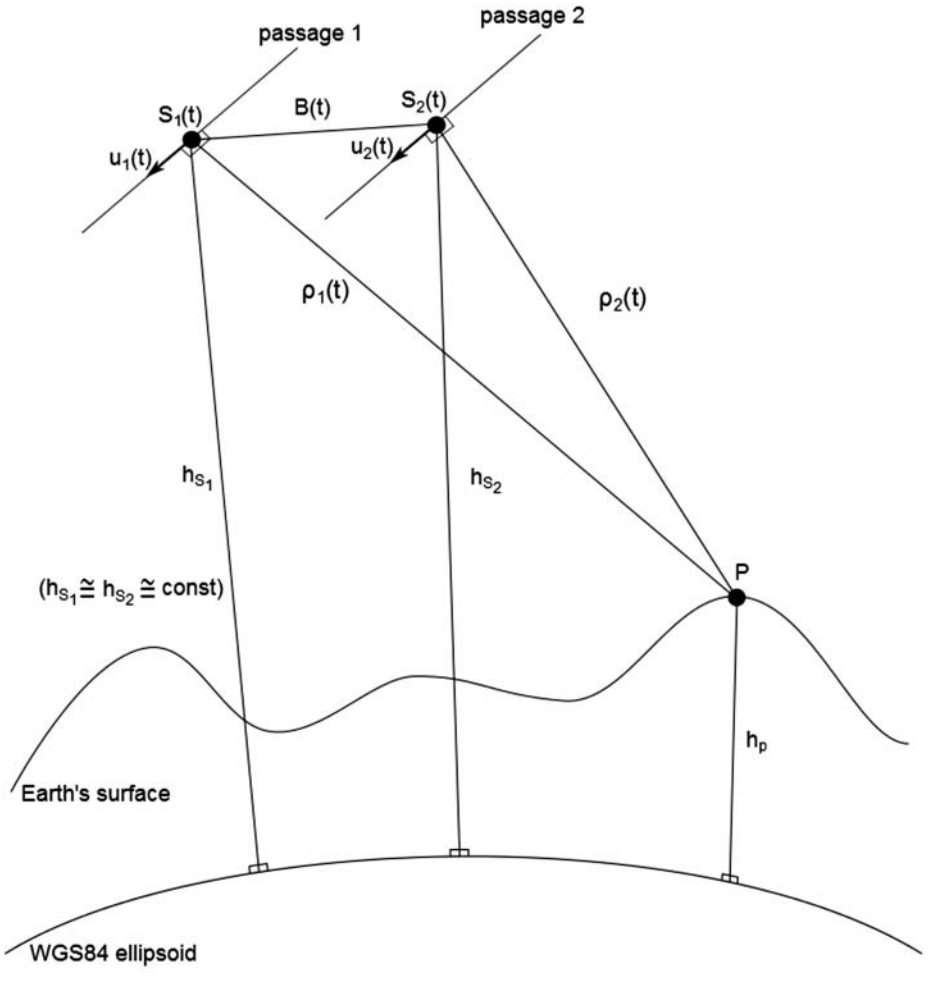

Figure 2. Geometry of common model in zero-Doppler configuration.

We also introduced the following quantities that have a role to play in representing the geometric configuration in the InSAR and radargrammetric approaches, respectively:

- $\mathbf{B}(t_1, t_2) = \mathbf{S}_2(t_2) - \mathbf{S}_1(t_1)$ is the baseline between the position of the sensor in the two passages,
- $\frac{B(t_1,t_2)}{\frac{1}{2}\left(h_{S_1}(t_1)+h_{S_2}(t_2)\right)} \simeq \frac{B}{h}$ is the base(line)-to-height ratio,

where $h_{S_1}(t_1)$ and $h_{S_2}(t_2)$, representing the WGS84 ellipsoidal heights of the sensor in the two passages, can be considered to be approximately equal to the common evaluation of this ratio. Moreover, both these quantities can be considered to be approximately constant over the acquisition interval for the most relevant geometric consideration in which they are contained.

Important to note is that, for radargrammetry, ρ_1 and ρ_2 are related to the slant range resolution (column spacing), as follows:

$$\rho_i = D_{S_i} + CS_i \cdot I_i, \tag{2}$$

$$\rho_2 - \rho_1 = (D_{S_2} + CS_2 \cdot I_2) - (D_{S_1} + CS_1 \cdot I_1), \tag{3}$$

where D_{S_i} is the so-called "near range" of the ith image and CS_i is the column pixel spacing which is related to the slant range resolution of the ith image, both known through metadata. I_1 is the measured column position of point P on the first image and $(I_1 - I_2)$ is estimated through image matching.

On the other hand, for the case of InSAR measurements, ρ_1 and ρ_2 are related to the measured phase difference, $\Delta\varphi_{12}$, between images, and to the unknown number, N_{12}, of the half wavelength, $\lambda/2$, estimated by phase unwrapping, as follows:

$$\rho_2 - \rho_1 = \frac{\Delta\varphi_{12}}{2\pi}\frac{\lambda}{2} + N_{12}\frac{\lambda}{2}. \tag{4}$$

Therefore, it is clear why image matching and phase unwrapping are so crucial for the two approaches.

4. Radargrammetric processing

In this section, the radargrammetric DSM generation procedure (implemented in SISAR) is discussed. Following customization of the common generic model (1) to this case, and in order to establish the so-called image orientation model, image matching is analysed in detail, by considering both theoretical aspects and experimental results. In this section, an individualized speckle denoising approach is introduced, as employed in our work, that enhances image matching, improving the DSM quality in terms of point density.

4.1. Orientation model

The radargrammetric model is just based on equations of the global common model (1). The radargrammetric approach performs a 3D reconstruction based on the determination of the sensor–object stereo model for which the position of each point on the object is computed as the intersection of two radar rays coming from different positions and, therefore, with two different look angles (figure 3).

Observing the target in the opposite-site view allows one to obtain good stereo geometry but causes large geometric and radiometric disparities that may reduce image matching. Thus, to increase the efficiency of the image-matching process that has a strong impact on DSM accuracy, a good compromise is to use a same-side configuration stereopair with a base-to-height ratio ranging from 0.25 to 2 (Méric et al. 2009) or, better, from 0.25 to 0.8.

Equations (1) can be rewritten omitting the epoch t of each satellite position and velocity to simplify the notation and explicitly specifying the slant range

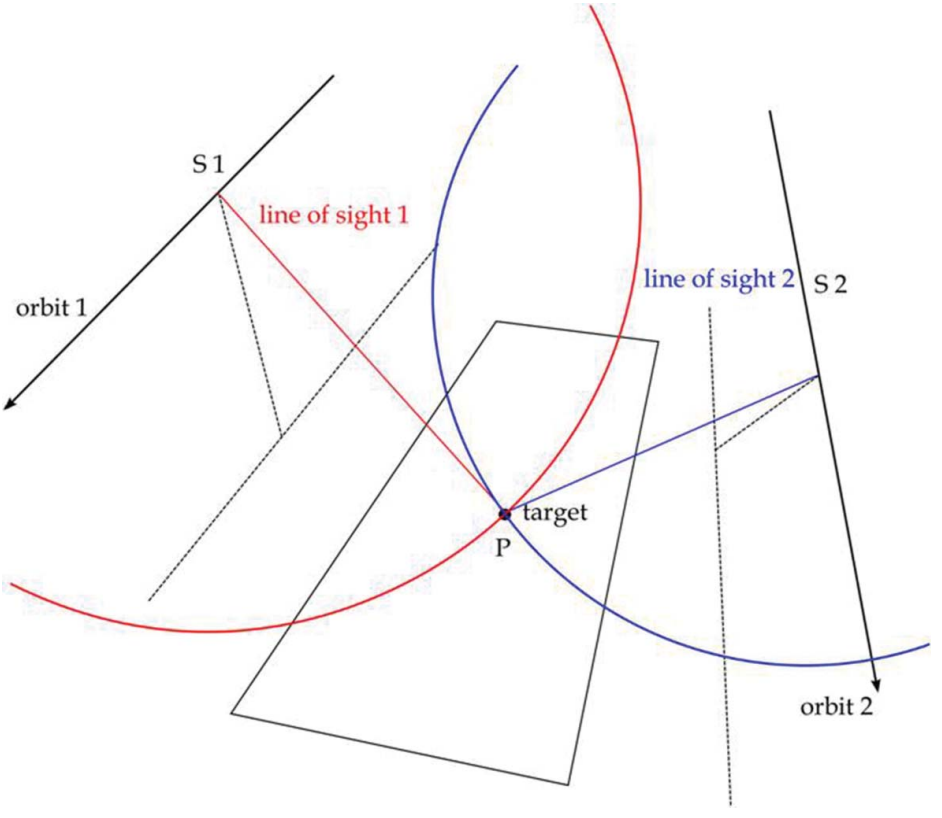

Figure 3. SAR acquisition system in zero-Doppler geometry.

measurement terms (Capaldo et al. 2011) as follows:

$$\begin{cases} u_{S_{X1}} \cdot (X_P - X_{S_1}) + u_{S_{Y1}} \cdot (Y_P - Y_{S_1}) + u_{S_{Z1}} \cdot (Z_P - Z_{S_1}) = 0 \\ \sqrt{(X_P - X_{S_1})^2 + (Y_P - Y_{S_1})^2 + (Z_P - Z_{S_1})^2} - (D_{S_1} + CS_1 \cdot I_1) = 0 \\ u_{S_{X2}} \cdot (X_P - X_{S_2}) + u_{S_{Y2}} \cdot (Y_P - Y_{S_2}) + u_{S_{Z2}} \cdot (Z_P - Z_{S_2}) = 0 \\ \sqrt{(X_P - X_{S_2})^2 + (Y_P - Y_{S_2})^2 + (Z_P - Z_{S_2})^2} - (D_{S_2} + CS_1 \cdot I_2) = 0 \end{cases} \quad (5)$$

In the case of SpotLight images, the orbital arc is quite short (approximately 10 km), such that it is conveniently represented by interpolating the orbital state vectors available in image metadata using Lagrange polynomials. In this way, it is possible to model image acquisition and stereo orientation directly on the basis of image metadata without the use of ground control points (GCPs). In fact, the satellite position is related to the acquisition time of each line of the image and can be computed using the acquisition start time and the pulse repetition frequency (PRF) (i.e. the sampling frequency in the azimuth direction); the values for these parameters are

also available in the metadata. Similar to the range case in (2), the linear relationship between the acquisition time, t_0, of each GP and its line number, J (6), can be expressed by the following linear relationship:

$$t = t_0 + \frac{1}{\mathrm{PRF}} J. \tag{6}$$

The model is simple and it is able to supply a good single image orientation. On the other hand, it displays slightly stiff behaviour in stereo restitution due to the lack of flexibility regarding the geometric intersection of the two radar rays. The model can also be a drawback if not enough accurate metadata are available (Schubert et al. 2012) because it results in a poor geometric intersection that hinders image matching and DSM generation.

The presented radargrammetric orientation model was conveniently parametrized using rational polynomial coefficients (RPCs). A tool for RPC generation, based on a so-called terrain-independent scenario, was implemented in SISAR (Crespi et al. 2010; Capaldo et al. 2012).

In table 2, the main parameters for the same-side radargrammetric stereopair are shown.

4.2. Image matching: the proposal of a novel strategy

An image-matching algorithm is able to select corresponding (homologous) points within (at least) two images of the same object acquired from different points of view (Ma et al. 2004). Two images are the main starting point of any image-matching process. Determining a matching entity, a so-called *primitive* (corresponding to a point) in one of the considered images (master image) as compared to the slave (other) image(s) in order to identify correspondences between them, depends on the selection of search criteria robust enough to limit possible solutions and avoid mismatching.

Although many matching approaches have been proposed in the literature, mainly for optical images (Heipke 1996), the development of a fully automatic, accurate, and reliable image-matching strategy is still a challenging problem for high-resolution SAR images. Dissimilarities between images due to the shadow effect, geometric distortion, radiometric differences, and speckle noise must be taken into account.

An original matching procedure, suited both for optical and for SAR imagery and presently under patent by the University of Rome "La Sapienza", was designed and implemented in SISAR (Nascetti 2013).

The first step of a SISAR image-matching procedure is the selection of an area of interest and a coarse height range (of approximate maximum and minimum terrain ellipsoidal heights) that allow the reduction of the object's space and a decrease in processing time. Subsequently, following image preprocessing, a regular 3D grid was generated for ground geometry using several layers of slicing over the entire height

Table 2. Same-side radargrammetric stereo geometry.

Baseline B (km)	255
Satellite height h (km)	620
Ratio B/h (–)	0.34

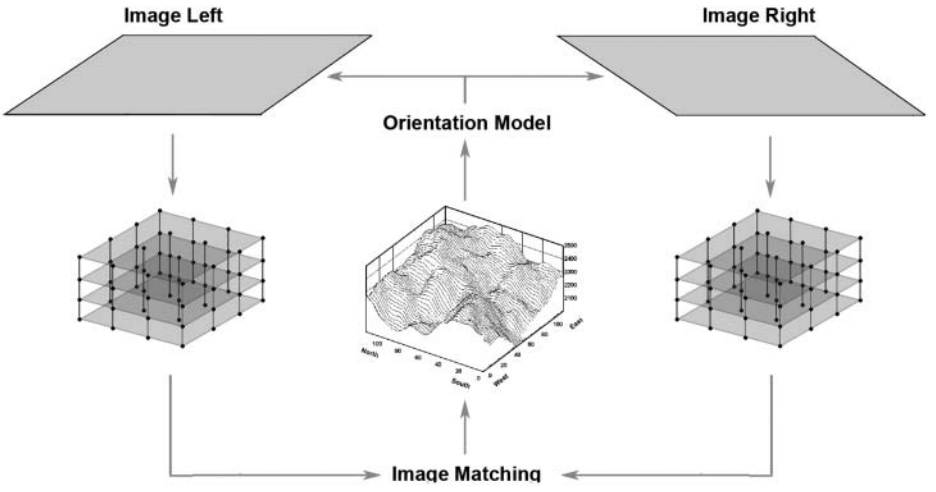

Figure 4. Geometrical constrain and voxel generation.

range. Beginning with this 3D grid, by means of the orientation model, stereo images were reprojected and on each layer created two voxel sets (one for the left and one for the right image). Using this process (figure 4), the two generated voxel sets contained geometrically corrected radiometric information within the same ground reference system.

At this point, for each horizontal position (X, Y) of the 3D grid, the main objective was to identify the correct height by comparing the two voxel sets. The correct height corresponds to best matching of the two voxels (for the left and right images) at the same height. Therefore, the search can be conveniently performed along vertical paths.

For detecting corresponding points (primitives), in the past, an area-based matching (ABM) criterion had been used and the signal-to-noise ratio (SNR) had been analysed (Ma et al. 2004). In this regard, the proposed algorithm uses the image orientation model in order to limit the search area of corresponding primitives, allowing fast and robust matching.

The matching strategy was applied in a coarse-to-fine hierarchical solution by resampling the two images according to a standard pyramidal scheme based on a multi-resolution approach. A well-known advantage of this technique is that at lower resolution it is possible to detect larger structures, whereas at higher resolutions, small details are progressively added to the already obtained coarser DSM. The procedure begins by choosing a suitable image multi-looking by considering the original image resolution.

Previous experimental results indicate strong noisy radiometric information of SAR imagery inherit to the matching process, and, consequently, the detected homologous points are not enough to generate a complete and dense DSM. Image denoising for speckle is, therefore, needed for successful matching. Additionally, within an urban area, the main features represented within the SAR image are due to the building double-bounce effect, and for imaging system geometry, the white line is mainly oriented to the azimuth direction (see figure 5 (top)). The phenomenon, as shown in figure 5 (bottom), leads to detected homologous points (blue dots), remarkably distributed along the azimuth direction.

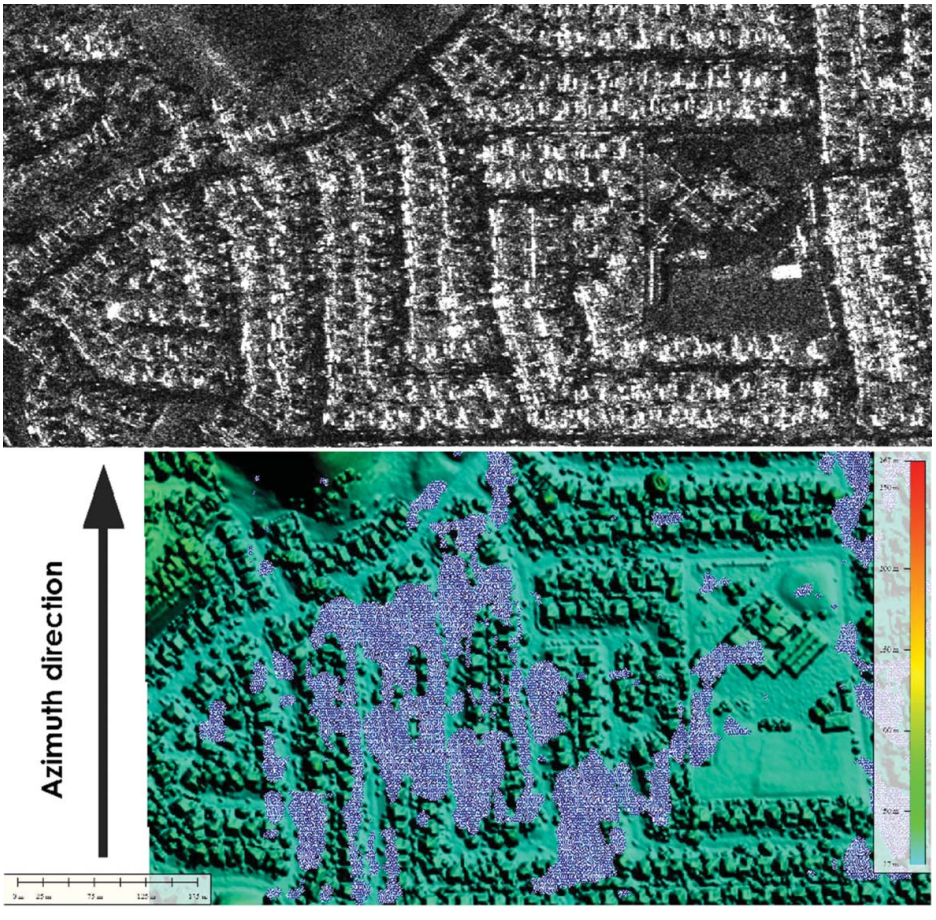

Figure 5. Comparison between power image and matched points (blue dots) over the LiDAR DSM.

4.3. Image speckle denoising

As previously mentioned, the imagery produced by SAR systems is degraded by the high level of noise inherent to radar backscatter. The largest source of noise is speckle noise, a result of coherent interference of waves scattered from the terrain elements observed in each resolution cell. In fact, the vast majority of surfaces, synthetic or natural, are extremely rough on the scale of an optical wavelength (Goodman 1976). Due to interference, both constructive (the sum of the intensities) and destructive (the difference in the intensities), of the electromagnetic waves reflected by the different objects illuminated by SAR, the intensity of each pixel is corrupted and leads to speckle displays (i.e. noise that determines the granular (the so-called *salt and pepper*) aspect of the image and prevents easy target recognition and texture analysis). Hence, speckle noise reduction is one of the crucial steps for increasing the quality of radar images.

To retrieve the unspeckled image from the observed one, it is necessary to adopt a model that relates the two entities, at each pixel, as a function of the speckle noise. The most commonly used model represents speckle as multiplicative noise, as follows:

$$I(t) = S(t) \cdot i(t), \tag{7}$$

where $I(t)$ is the observed intensity of the pixel located at t, $S(t)$ is the terrain reflectivity (unspeckled reflectivity), and $i(t)$ is the intensity of fully developed speckle noise.

The various filtering techniques were developed into two different domains: a frequency domain and a spatial domain. In the frequency domain, the windowing process was used (i.e. a convolution between the frequency transform of the image and the frequency transform of the filter). In the spatial domain, the noise could simply be removed using a low pass filter (e.g. by smoothing an image). However, speckle radar noise requires more involved techniques such as adaptive filters that allow the preservation of image sharpness, edges, and point features suppressing noise.

We chose to use filters in the spatial domains, while considering some preliminary experiments where better than frequency-domain filters were used. The most well known filters belonging to this category were Lee, Kuan, GammaMAP, and similar filters (Mansourpour et al. 2000). All are represented by a kernel (i.e. an array that is multiplied or added to each pixel [and its surrounding values] within an image). In most applications, the kernel is represented by a square with an odd number of elements in each dimension, and its centre is sequentially aligned until the entire image has been covered with a current pixel that holds the new calculated value.

We developed an original filtering procedure to maximize not only the number of points, but also their statistical goodness. Unlike traditional preprocessing techniques, image filters were made by directly using an image-matching procedure, including implementing filtering algorithms into the main SISAR software. The procedure allowed us to operate at several pyramidal levels independently and in different ways (e.g. making one or more filtering cycles on the respective image). The effect of GammaMAP filter smoothing is shown in figure 6, displaying noisy (left) and filtered (right) images.

Figure 6. Effect of GammaMAP filtering: noisy image (left) and filtered image (right).

4.4. Point cloud interpolation

In general, the output of a matching procedure is a 3D point cloud. To obtain a regular gridded DSM, a procedure able to interpolate such sparse data is necessary. Several interpolation methods such as kriking, the nearest or natural neighbour, polynomial regression, moving average, and splines have been developed. For our study, a moving average method was chosen in order to reduce a portion of the radargrammetric DSM high frequencies that are due to residual speckle noise following filtering. By averaging data within the grid node's search circle, the method assigns values to the grid nodes, provided that a minimum number of points (here eight) are available (Yang et al. 2004).

5. Interferometric processing

In this section, the InSAR DSM extraction procedure (implemented in SARscape®) is discussed. The technique requires the following steps: a baseline estimation and geometric assessment, an imagery coregistration, interferogram generation, interferogram filtering, phase unwrapping, phase to height conversion, and geocoding. As before, the model used in the final step was customized from the general model previously presented.

5.1. Preliminary concepts: baseline and coherence estimation

At first, to evaluate the quality of the geometric configuration, the baseline between the interferometric images was estimated to compute the 2π ambiguity (table 3), also called the altitude ambiguity (Hanssen 2001; Ferretti et al. 2007), as follows:

$$h_a = \frac{\lambda R \tan(\theta)}{2B}. \tag{8}$$

The complex coherence, γ, between the two variables y_1 and y_2 was considered, defined as follows:

$$\gamma = \frac{E\{y_1 y_2^*\}}{\sqrt{E\{|y_1|^2\}E\{|y_2|^2\}}}, \quad 0 \le \gamma \le 1. \tag{9}$$

A coherence value can be assigned to every pixel within the interferogram. The coherence can be used as a measure of the accuracy of the interferometric phase. Ideally, expectation values in equation (9) are obtained using a suite of observations for every single pixel. Unfortunately, since every full-resolution pixel is observed only

Table 3. Baseline and ambiguity height information.

Normal baseline (m)	741.576
Critical baseline (m)	10348.777
2π ambiguity height (m)	5.389

once during each SAR acquisition, this procedure is not feasible. In practical situations, the accuracy of the phase observations of a uniform region is assumed to be stationary. Under the assumption of ergodicity, it is possible to exchange ensemble averages with the spatial averages obtained over a limited area surrounding the pixel of interest. Such as assumption is used to obtain the maximum-likelihood estimator of the coherence magnitude, $|\widehat{\gamma}|$, over an estimation window of N pixels (Seymour & Cumming 1994):

$$|\widehat{\gamma}| = \frac{|\sum_{n=1}^{N} y_1^{(n)} y_2^{*(n)}|}{\sqrt{\sum_{n=1}^{N} |y_1^{(n)}|^2 \sum_{n=1}^{N} |y_2^{(n)}|^2}.} \tag{10}$$

As shown in table 4 and figure 7, imagery coherence results were, on average, higher than 0.5. The higher the coherence value (maximum 1), the more similar backscattered signal characteristics between the two images, making it easier to subtract phase information related to the scatterer's dielectric properties during the subsequent interferogram generation step. In figure 8, a coherence map of the San Francisco area is shown. The map was evaluated by computing the absolute value of γ on a moving window spanning the entire SAR image. In addition to high coherence in urban areas, deserted areas also appeared brighter than vegetated ones, indicating higher coherence values. On the other hand, a loss of coherence on lakes (dark in the image), due both to daily changes and to the almost specular reflection of

Table 4. San Francisco coherence map statistics (m).

Minimum	Maximum	Mean	Standard deviation
0.001	0.960	0.533	0.151

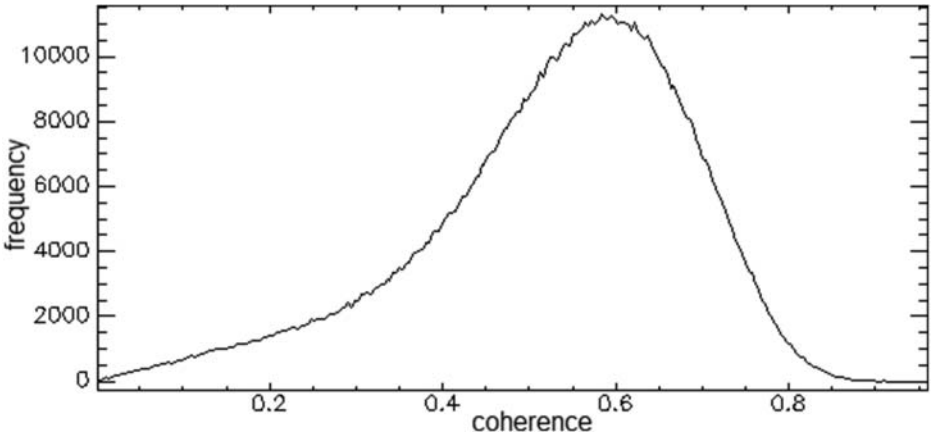

Figure 7. Histogram of coherence values.

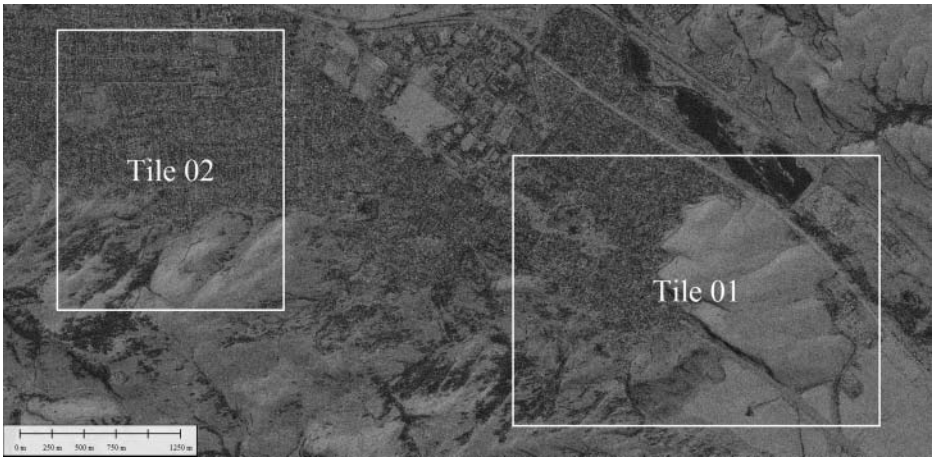

Figure 8. San Francisco coherence map.

electromagnetic waves over flat surfaces, was evident, and implied no backscattering returns, thereby leading to a low SNR for the corresponding pixels in SAR images.

5.2. *Coregistration*

The two images were acquired from different points of view and at different distances, and so were rotated, shifted, and scaled relative to one another. Sub-pixel registration of both focused SAR images was a strict requirement for interferometric processing. Coregistration is the process of superimposing, in slant range geometry, two or more SAR images. The first image is called the *master*, while the superimposed second image(s) the *slave*. The processing step is performed in the following stages:

- A local non-parametric shift is estimated on the basis of the orbital data and a known DEM (e.g. SRTM3 [3×3 grid posting], as in our case). In the event of inaccurate orbits, a large central window (cross-correlation central window) is used. A set of windows (cross-correlation grid) is determined on the master image. Then, the cross-correlation function is computed for each window with its maximum indicating the proper shift for the selected location.
- The residual parametric shift, summed to the local non-parametric one, is calculated using a polynomial interpolation that depends on the azimuth and range pixel positions. In the event the input SAR data are represented by single look complex (SLC) products, the residual parametric shift is further refined by computing mini-interferograms on small windows (fine shift parameters) distributed throughout the image.

5.3. *Interferogram generation and filtering*

After image coregistration, an interferometric phase (φ) is generated by multiplying one image by the complex conjugate of the second one. To simplify phase unwrapping, phase information due to topography is removed on the basis of a known

DEM by producing a "synthetic" phase from a known DEM. The resultant interferometric phase is as follows:

$$\phi_{\text{int}} = \phi_{\text{topo,res}} + \phi_{\text{scatt,res}} + \phi_{\text{atm,res}} + \phi_{\text{noise}}, \tag{11}$$

where $\phi_{\text{topo,res}}$, $\phi_{\text{scatt,res}}$, $\phi_{\text{atm,res}}$, and ϕ_{noise} are the residual contribution from, respectively, topography, backscattering properties, the atmosphere, and processing noise. In figure 9, it is possible to observe the difference between the right-half image interferometric fringes (hill) and the left-image ones (urban area). The interferometric phase is characterized by values between $-\pi$ and π, and the already mentioned ambiguity of N integer cycles solved within the unwrapping step.

After removing the topographic synthetic phase, the interferogram can be filtered to obtain a smoother profile that is easier to process in the phase-unwrapping step. In this work, an adaptive Goldstein filter was employed. The variable bandwidth of the filter, derived directly from the power spectrum of the fringes, preferentially

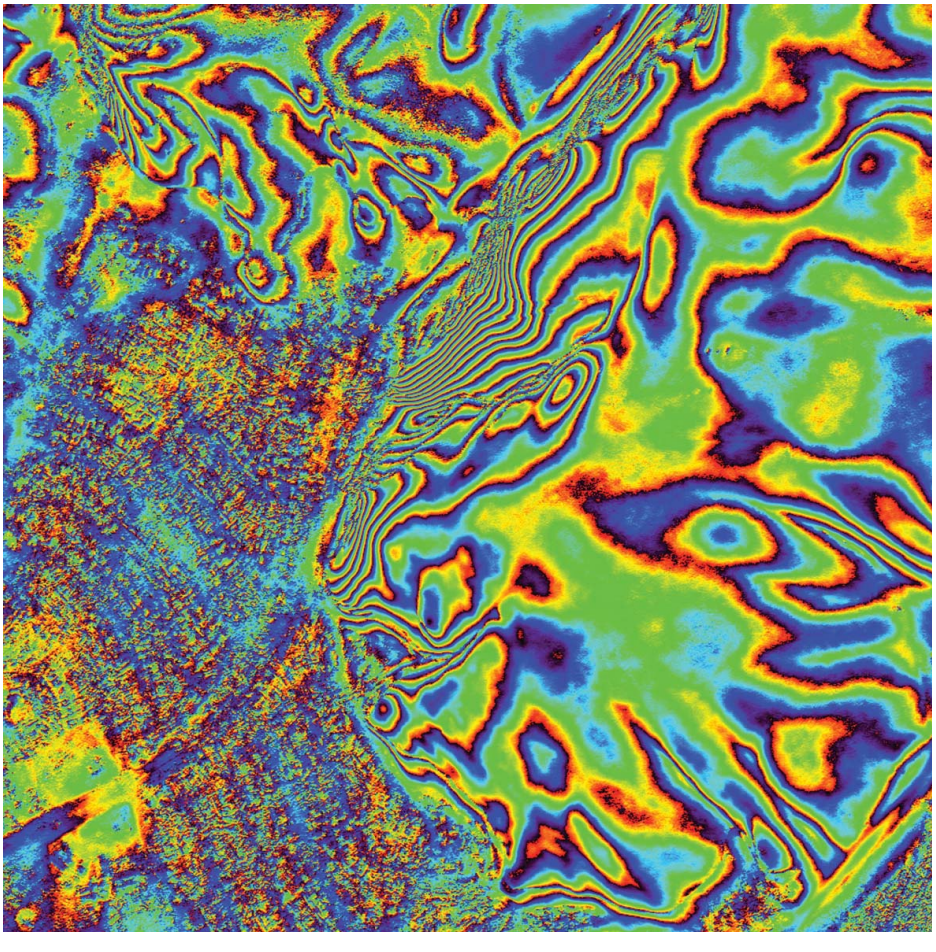

Figure 9. Filtered interferogram – tile 1.

smooths the phase in regions with a high correlation, but remains broad-band in regions where the correlation is low.

5.4. Phase unwrapping

The aim of the phase-unwrapping step is to solve the 2π ambiguity of the interferometric phase. Phase unwrapping is one of the main difficulties in radar interferometry, due to its inherent non-uniqueness and non-linearity. Variable phase noise, as well as geometric problems such as foreshortening and layover, is the main reason why many proposed techniques do not perform as desired. In the past, a minimum cost flow algorithm had been used. The method exploits the fact that discrete derivatives of the unwrapped phase are estimated possibly with an error that is a multiple of 2π, leading to a formulation of the phase-unwrapping problem as a global minimization problem with integer variables. The weighted deviation between the estimated and unknown discrete derivatives of the unwrapped phase is minimized, and is subject to the constraint that the two functions must differ by multiples of 2π (Costantini 1998). In figure 10, a sample unwrapping process is shown, taken from the case of study, over the hill of figure 9.

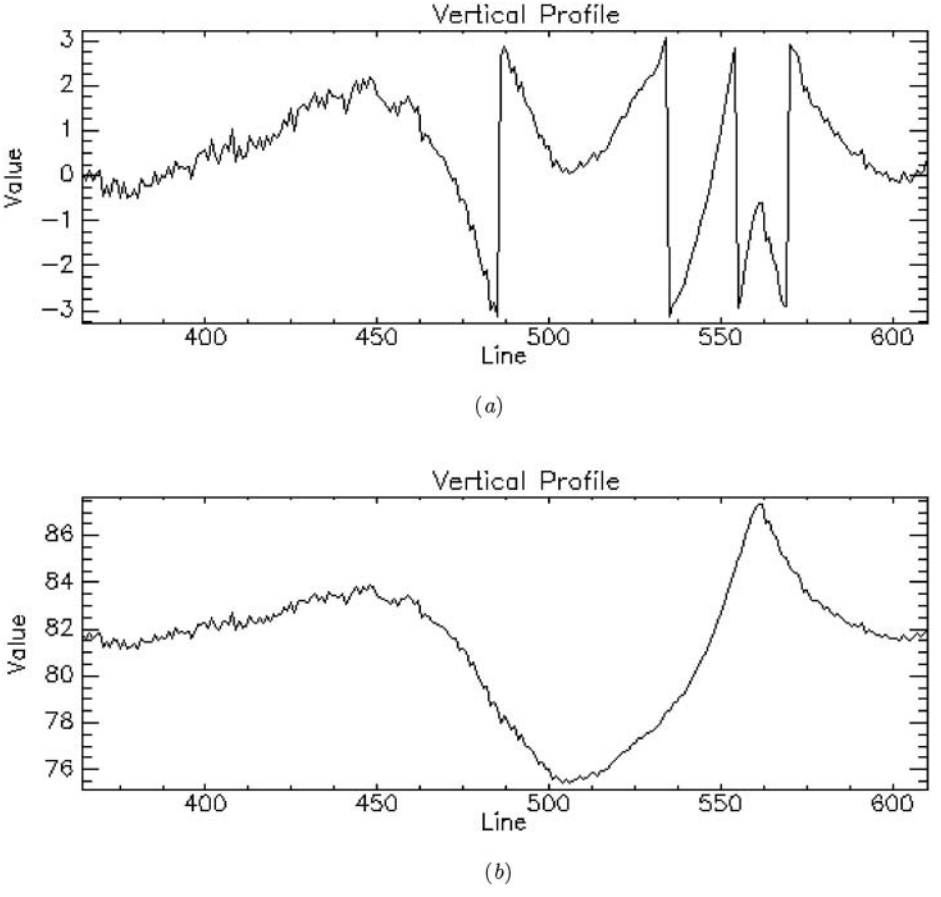

Figure 10. Phase-unwrapping example. (a) Interferogram (wrapped phase). (b) Unwrapped phase.

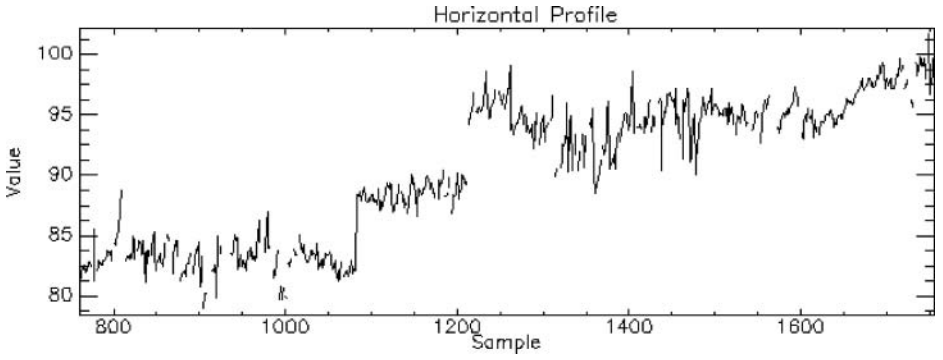

Figure 11. Wrong unwrapped phase. Two jumps are visible, at samples 1080 and 1200.

Phase unwrapping is the most critical step. Even if unwrapping algorithms can work well locally, when considering the larger scale, they can easily miss phase ambiguity resolution. Therefore, generating errors proportional to the height of ambiguity are shown in table 3. The errors are clearly visible over the second evaluated tile, where the unwrapping algorithm failed. In figure 12, the interferometric phase is visible, while in figure 11, a profile for the unwrapped phase is shown. Two shifts are clearly visible and are approximately equal to 2π.

5.5. *Phase to height conversion and geocoding*

The unwrapped phase is calibrated absolutely through the georeferencing constraint to (at least) one known GCP P_{ref} and re-summed to the synthetic phase, leading to customization of the common generic model (1), as follows:

$$\begin{cases} \rho_2 - \rho_1 = \dfrac{\Delta\varphi_{12}}{2\pi}\dfrac{\lambda}{2} + N_{12}\dfrac{\lambda}{2} \\ \mathbf{u}_1(t_1)\cdot(\mathbf{P} - \mathbf{S}_1(t_1)) = 0 \\ \mathbf{u}_2(t_2)\cdot(\mathbf{P} - \mathbf{S}_2(t_2)) = 0 \end{cases} \tag{12}$$

under the following constraints:

$$\begin{cases} \rho_{\text{ref}} = |\mathbf{P}_{\text{ref}} - \mathbf{S}_{\text{ref}}(t_{\text{ref}})| \\ \rho_1 - \rho_{\text{ref}} = \dfrac{\Delta\varphi_{ref1}}{2\pi}\lambda + N_{\text{ref1}}\lambda \end{cases} \tag{13}$$

where ρ_1, ρ_2, and ρ_{ref} are expressed in ECEF coordinates. The first constraint represents the phase's absolute calibration with respect to P_{ref}. The second one represents the transfer of this calibration over the entire interferogram, performed technically by re-summing the synthetic phase based on the coarse known DSM.

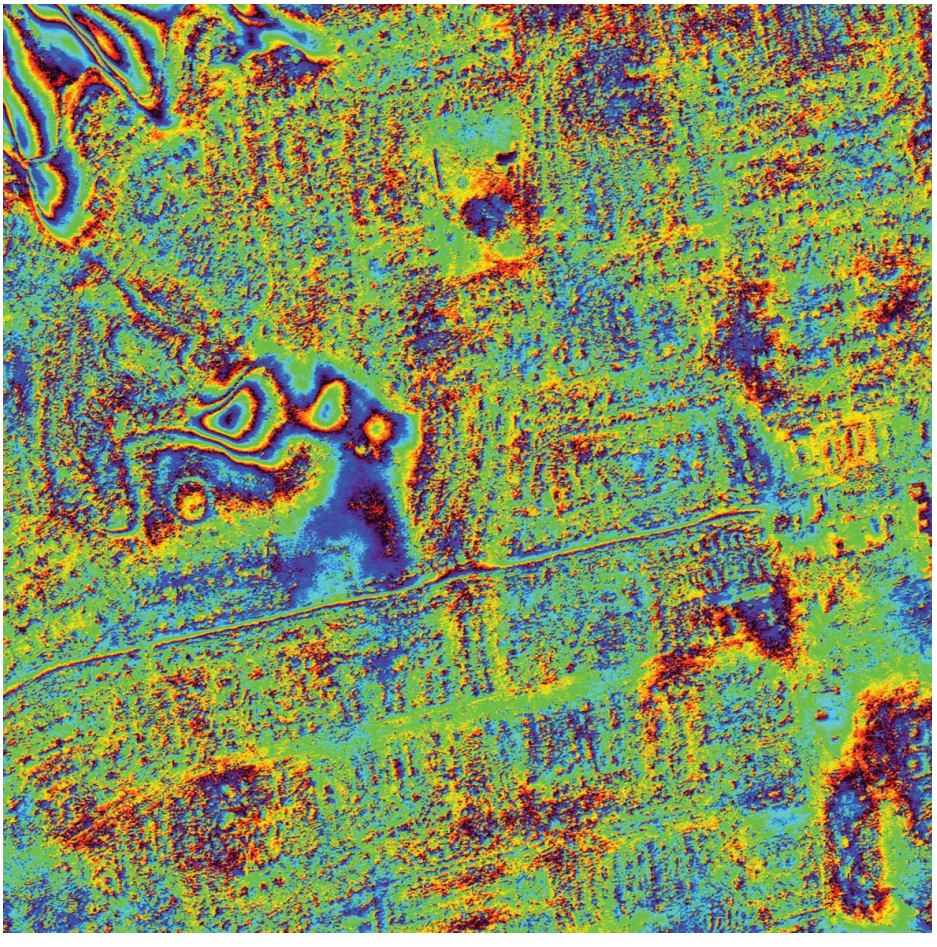

Figure 12. Residual phase of the second evaluated area.

6. DSM comparison and assessment results

InSAR DSMs were extracted using SARscape®, one of the most recognized commercial software packages for interferometric image processing, and tests were performed in collaboration with the image analyst of sarmap SA. For interferometric DSM generation, the SRTM DEM is necessary in order to remove the synthetic topographic phase, whereas it is not a mandatory requirement for the radargrammetric approach. Independence from any kind of *a priori* data is an advantage for the last technique in areas where the SRTM is not reliable or not available. Nevertheless, since the SRTM has been employed for the InSAR processing and to make a strict comparison between the two techniques, radargrammetric point clouds were filtered through the SRTM data. In particular, as a low texture area impacted by some spike errors (high local eight discrepancies), height differences between the point cloud and the SRTM were computed and points with values higher than 50 m were filtered out of the data. Then, a quality assessment of the filtered gridded radargrammetric DSM was performed and the advantage introduced by this filtering evaluated.

The accuracy assessment of the two DSM tiles with an extension of 2–3 km was performed using DEMANAL software. Height differences were computed by interpolating, using a bilinear method, the analysed DSM over the reference LiDAR DSM. The value was negative when the extracted DSM was above the reference LiDAR DSM. Accuracy, in terms of the RMSE, was computed at the 95% probability level (RMSE LE95) after evaluating the LE95. Therefore, the largest outliers were filtered out of the data.

In tile 1, as shown in table 5, global accuracy in terms of the RMSE was approximately 5 m, both for the interferometric and for the radargrammetric DSMs, whereas the filtered one provided a better RMSE value of 4.5 m and a decreased LE95 value of more than 2.5 m with respect to the original one, indicating the effectiveness of outlier filtering using the SRTM. Histograms of the discrepancies (DZ) (see figure 13) highlight some of the differences between the DSMs' error distributions. Radargrammetric DSMs presented a greater error in particular areas, whereas the InSAR DSM indicated a slight bimodal error distribution with a lower but evident second peak, as shown in figure 13. The relative error was evaluated up to a

Table 5. Tile 1: comparison between the evaluations of interferometric and radargrammetric DSMs.

DSM	N_Points	RMSE (m)	Standard deviation (m)	Bias (m)	LE95 (m)	Maximum (m)	Minimum (m)
InSAR	662,457	5.00	4.84	1.23	12.31	39.91	−68.25
Radargrammetric	664,566	5.01	5.01	−0.23	15.27	68.62	−68.82
Filtered radargrammetric	664,566	4.56	4.56	0.21	12.71	52.21	−67.48

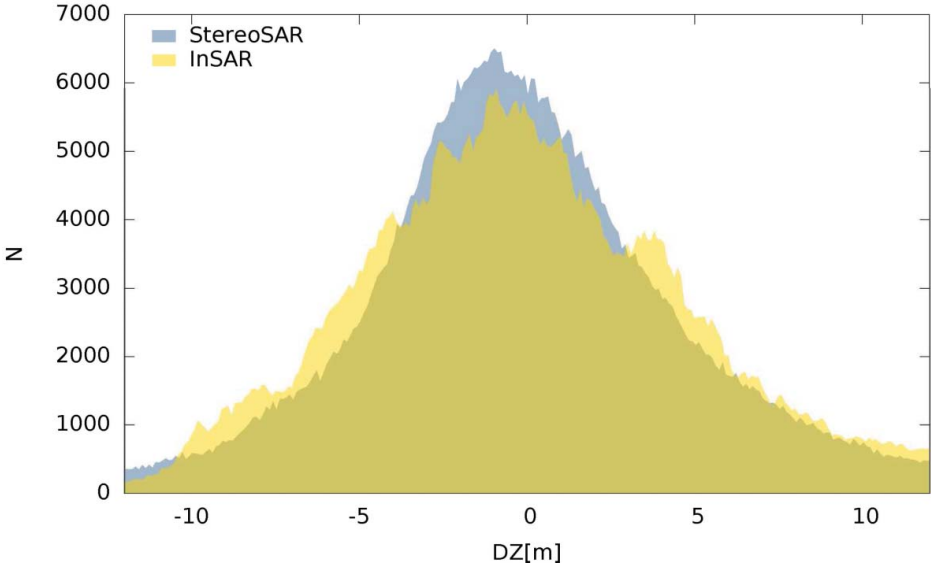

Figure 13. Tile 1: interferometric and radargrammetric error distribution.

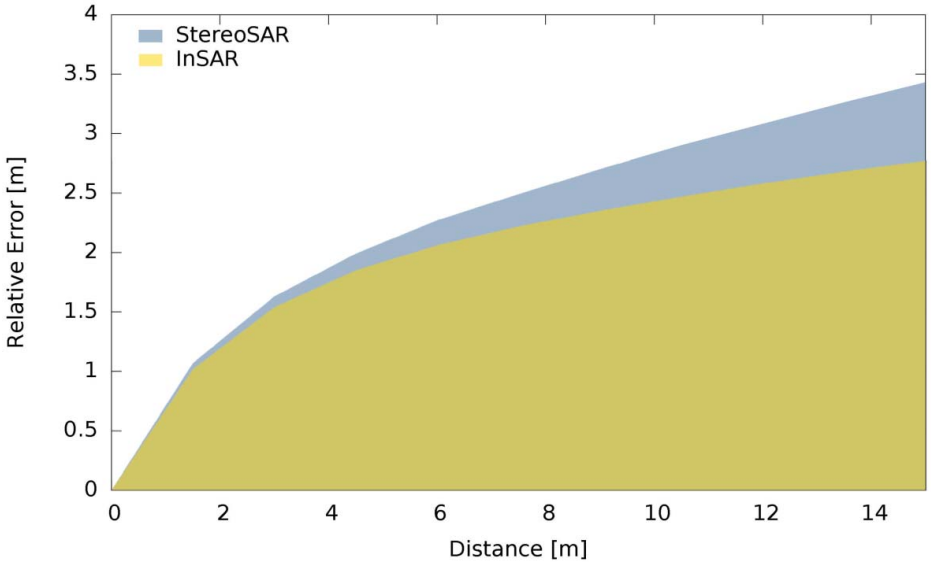

Figure 14. Tile 1: interferometric and radargrammetric relative error.

distance of 10 LiDAR DSM cells, that is, 15 m (see figure 14), and grew to approximately 3.0 m for the radargrammetric DSM and was slightly better (up to 2.5 m) for the InSAR DSM.

As shown in table 6, in tile 2, accuracy in terms of the RMSE was approximately 5.5 m for the interferometric DSM and again approximately 5 m for radargrammetric DSMs. Additionally, for the radargrammetric DSMs, the statistical LE95, MAX, and MIN were remarkably lower than for tile 1, such that less extreme value errors (outliers) were present. Such a result could be a possible explanation for the ineffectiveness of SRTM filtering for tile 2.

Based on figure 15, it is evident that the InSAR DSM histogram has an approximate three-modal distribution, likely due to the unresolved phase ambiguity. In regard to radargrammetric DSMs (figure 15), the histogram was characterized by an asymmetric narrow bell shape, a consequence of the prevalence of areas with positive errors (the error is positive when the reconstructed height is lower with respect to the reference DSM). Finally, the relative errors were computed and essentially had the same behaviour of tile 1 (see figure 16).

Table 6. Tile 2: comparison between the evaluations of interferometric and radargrammetric DSMs.

DSM	N_Points	RMSE (m)	Standard deviation (m)	Bias (m)	LE95 (m)	Maximum (m)	Minimum (m)
InSAR	457555	5.42	4.26	3.36	9.01	46.8	−24.61
Radargrammetric	434045	4.87	4.87	0.15	13.88	45.98	−30.22
Filtered radargrammetric	434045	4.91	4.86	0.71	13.61	42.70	−27.12

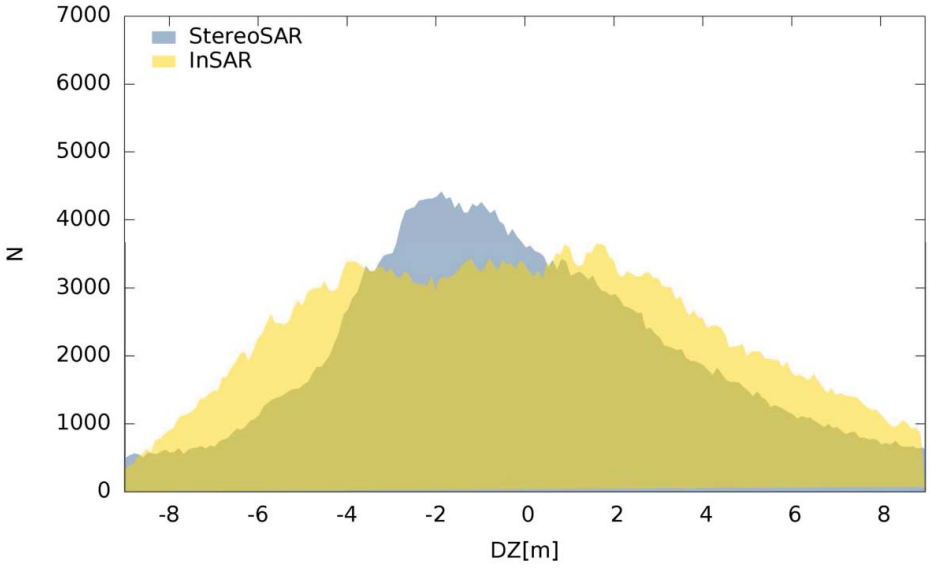

Figure 15. Tile 2: interferometric and radargrammetric error distribution.

To analyse and characterize morphological information useful for hydrological and hydrogeological risk studies (e.g. stream network identification), statistical evaluation of DSM accuracy in terms of the RMSE is not enough. Therefore, a deeper visual investigation was performed by investigating interferometric and radargrammetric (only the filtered one) error maps and the relative profiles. Regarding tile 1 in figure 17(*a*) and 17(*b*), the interferometric and radaragrammetric DSMs, as well as

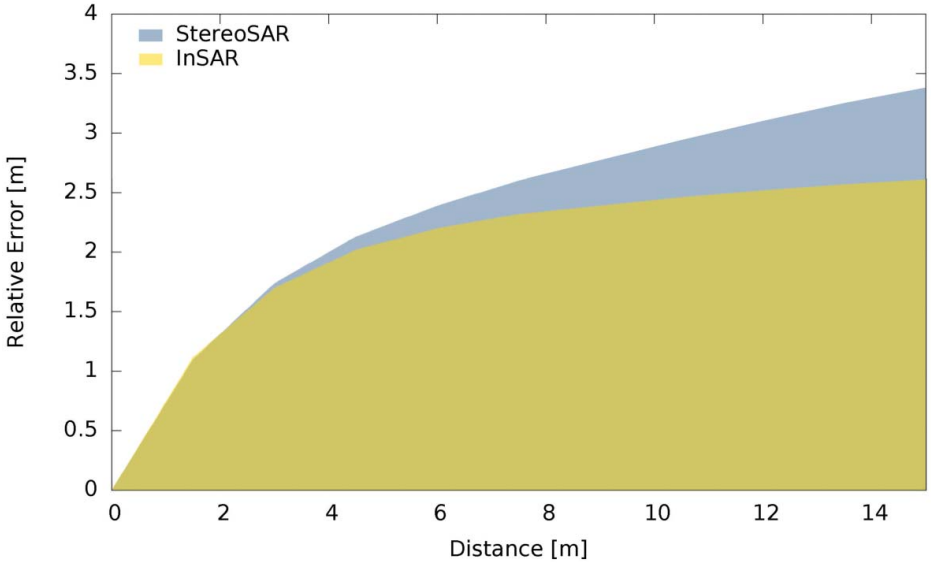

Figure 16. Tile 2: interferometric and radargrammetric relative error.

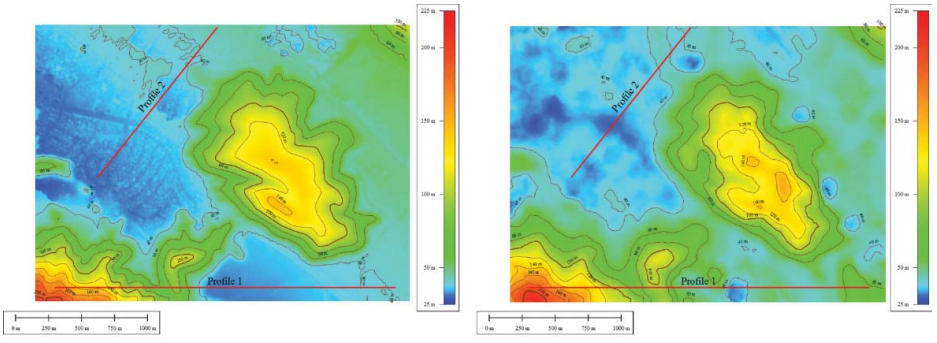

(*a*) (*b*)

Figure 17. Tile 1: interferometric and radargrammetric DSMs. (a) Interferometric DSM. (b) Radargrammetric DSM.

the two studied profiles, are shown. The former was chosen on a forested and desert area, and the latter within a mainly urban area. At first glance, it is clear that the interferometric DSM allowed us to detect more details, especially within the urban zone. Additionally, from error maps (see figure 19(*a*) and 19(*b*)) it is evident that the InSAR error was only distributed in specified zones (forested areas), whereas the radargrammetric distribution error was characterized by holes and patches, mostly in areas characterized by a lack of texture (such as a bare desert hill). In fact, within these areas it was difficult to match enough points to correctly reconstruct the morphology of the 3D terrain. Nevertheless, comparing interferometric and radagrammetric first profiles (see figure 18(*a*) and 18(*c*), respectively), it is clear that the former displays a ramp, likely due to the presence of a systematic error in orbit modelling

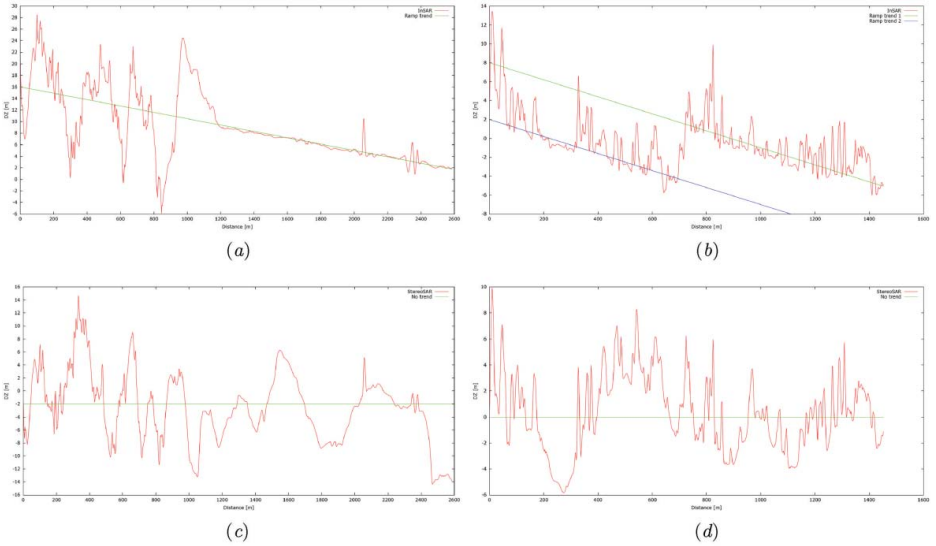

(*a*) (*b*)

(*c*) (*d*)

Figure 18. Tile 1: interferometric and radargrammetric map error profiles. (a) Interferometric profile 1. (b) Interferometric profile 2. (c) Radargrammetric profile 1. (d) Radargrammetric profile 2.

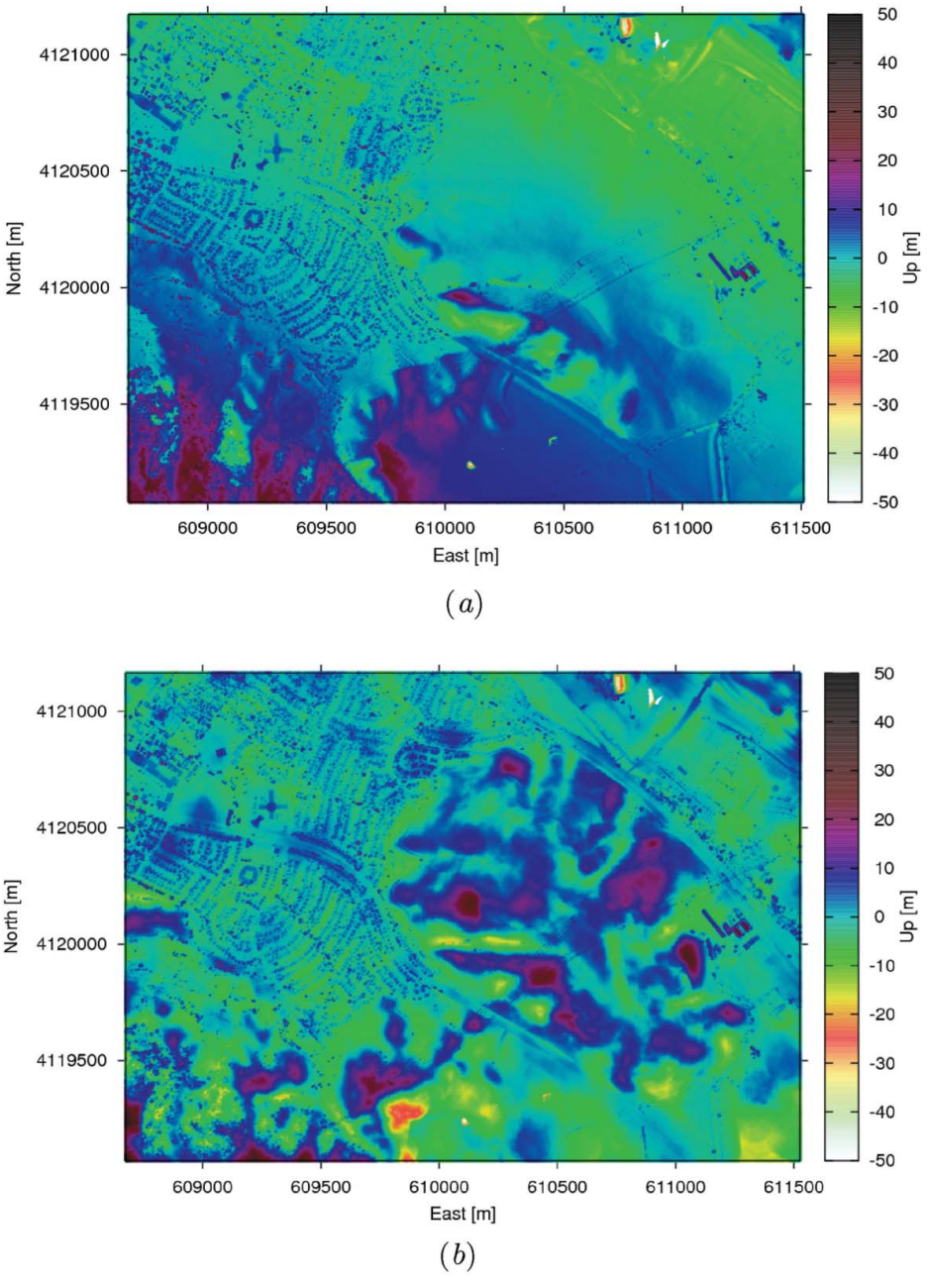

Figure 19. Tile 1: interferometric and radargrammetric error maps. (a) Interferometric error map. (b) Radargrammetric error map.

and absent in the latter which indicates noise, but that is a flat medium trend with only a slight bias. For the second profile, the effect is similar (see figure 18(*b*) and 18(*d*)). Also evident is that a step between the two interferometric ramps, whose value is very close to the 2π altitude ambiguity (of approximately 5.5 m), is likely due to a residual phase jump, not corrected during phase unwrapping.

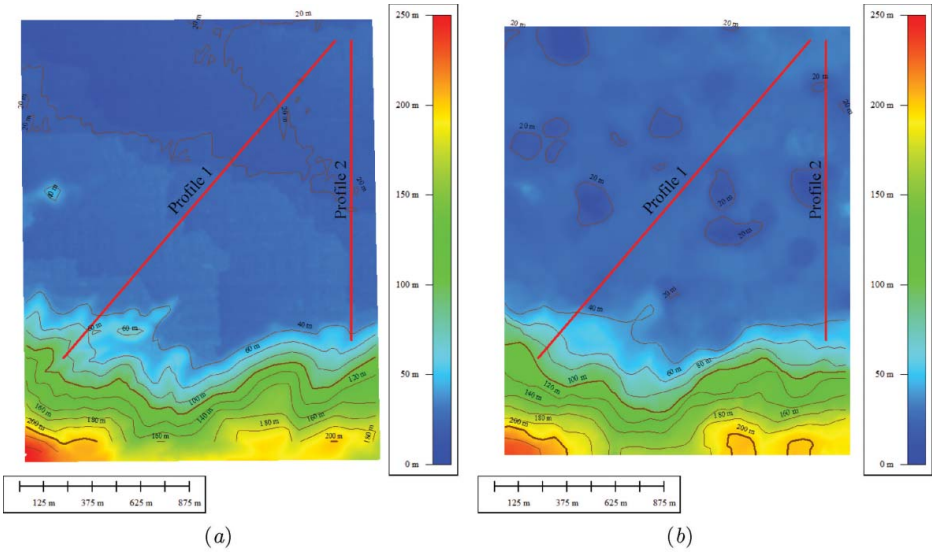

Figure 20. Tile 2: interferometric and radargrammetric DSMs. (a) Interferometric DSM. (b) Radargrammetric DSM.

Such errors in both interferometric and radargrammetric DSMs could represent obstacles for successfully carrying out hydrological and hydrogeological risk analyses and must be carefully considered.

Tile 2 in figure 20(*a*) and 20(*b*) provides the interferometric and radargrammetric DSMs, and both the profiles chosen belonged to the urban area, but with different directions. Even for this area, the InSAR DSM seems to reconstruct the features

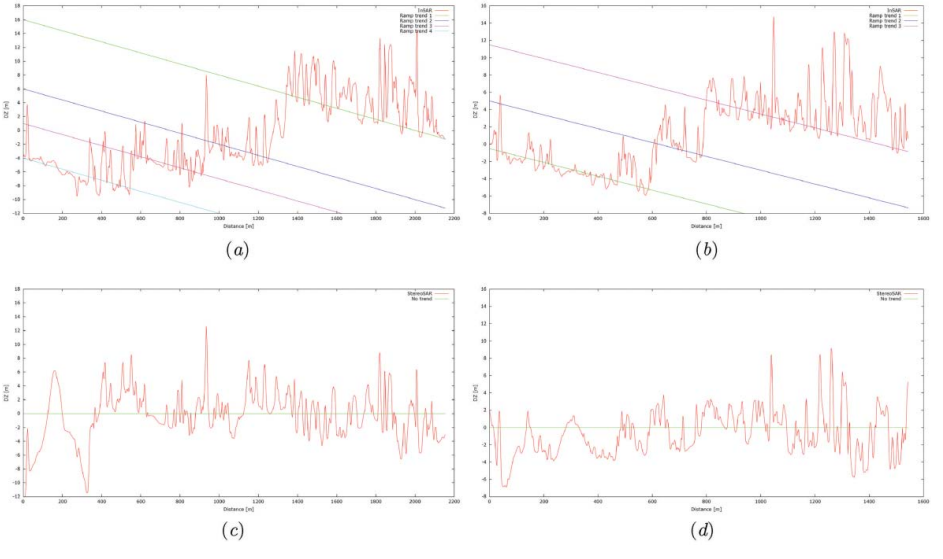

Figure 21. Tile 2: interferometric and radargrammetric map error profiles. (a) Interferometric profile 1. (b) Interferometric profile 2. (c) Radargrammetric profile 1. (d) Radargrammetric profile 2.

better than the radargrammetric one, and the error maps indicate a height difference distribution (see figure 22(*a*) and 22(*b*)). Interferometric systematic errors are concentrated in areas where coherence is lower, and radargrammetric random errors where there is a lack of texture. From the first interferometric profile, the presence of four ramps and consequently three steps (see figure 21(*a*)), whose magnitudes are quite

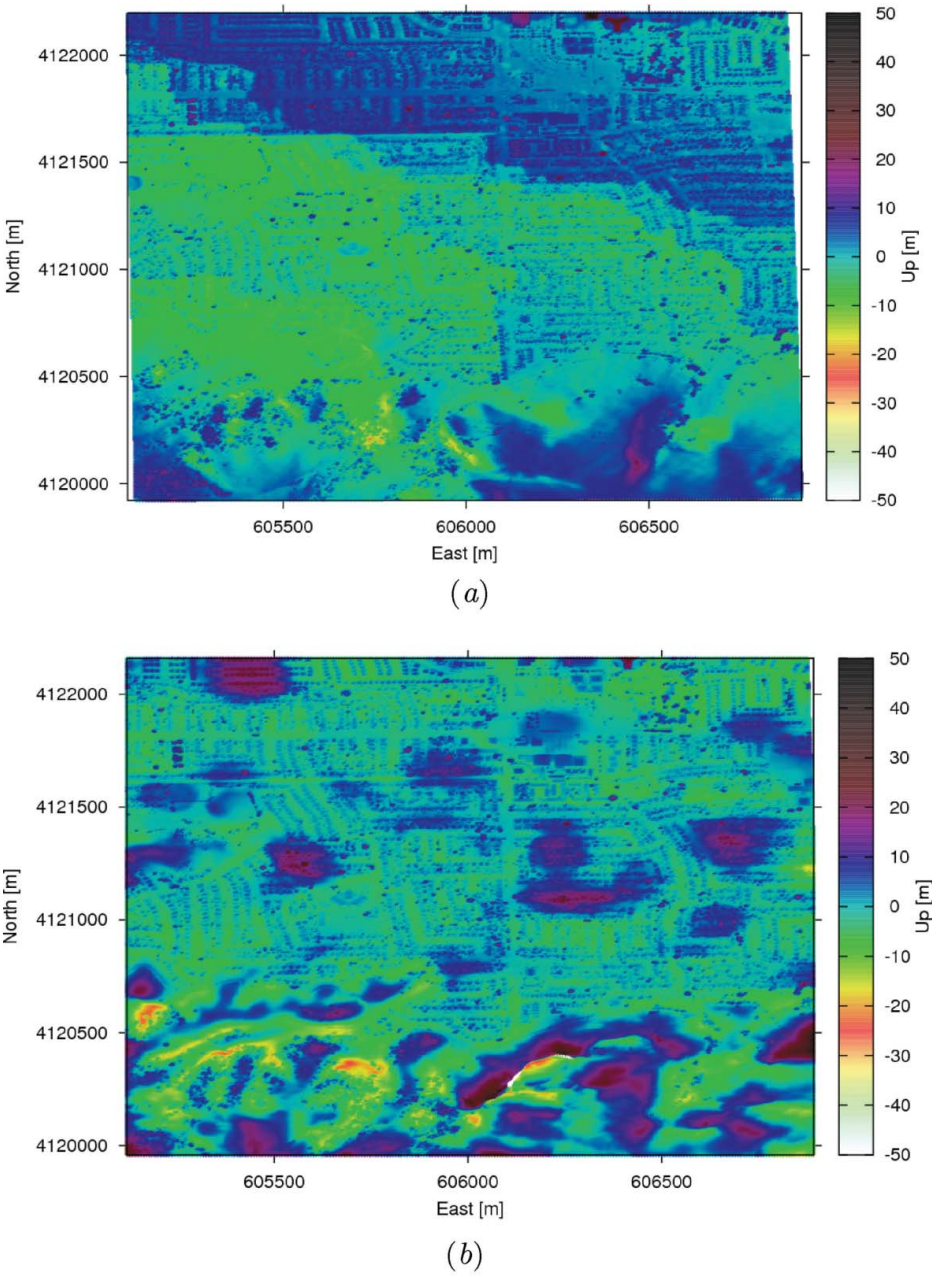

Figure 22. Tile 2: interferometric and radargrammetric error maps. (a) Interferometric error map. (b) Radargrammetric error map.

close to the 2π altitude ambiguity of approximately 5 m (the last at approximately 10 m is likely due to two cycle jumps), is strongly evident. A similar result can be determined for the second profile (see figure 21(*c*)) where three different ramps and two steps of approximately 5 m are easily detected. The features are completely absent in radargrammetric profiles (see figure 21(*b*) and 21(*d*)) such that even if they are characterized by several types of noise, they have a flat pattern without bias and jumps.

7. Conclusions and future work

We began by evaluating the strengths and weaknesses of interferometric and radargrammetric approaches by looking at SAR's capability for producing DSMs suitable for hydrological and hydrogeological studies. Our first consideration was related to the importance of the data needed for processing. Various land cover types had a strong impact on our results using the two approaches. Interferometry was significantly influenced by low coherence due to vegetation, air humidity, atmospheric conditions, the temporal acquisition distance, and the complexity of interferometric fringes. Radargrammetry is not useful in areas with poor texture where matching is more difficult and generally supplies a less complete DSM. Interferometry was also characterized by a complex processing chain, hardly influenced by several processing parameters (input DEM for flattening, filtering parameters, GCP's positioning, and, last but not least, unwrapping algorithm parameters). Radargrammetric processing seemed to be more robust and straightforward and did not strictly require an *a priori* known DEM. Moreover, radargrammetry, taking advantage of intrinsic SAR imagery geolocation, allowed us to generate DSMs without using GCPs or other ground information, in contrast to InSAR that requires a DEM *a priori* product (currently, SRTM DEM is used to help during the unwrapping step). Both approaches presented critical issues within the processing chain: phase unwrapping for InSAR and the image-matching procedure for radargrammetry. Our comparison was performed by evaluating the interpolated DSMs extracted using the interferometric and radargrammetric techniques. Over the San Francisco test site, using SpotLight imagery with the two techniques, we obtained comparable DSM accuracies (root mean square error [RMSE]). Moreover, to further investigate the information supplied for hydrological and hydrogeological risk studies (e.g. stream network identification), DSM error maps and their relative profiles were produced. A comparison indicated differences in the morphology terrain reconstruction: radargrammetric DSMs led to zones with holes and strong noise, but also with a flat medium trend for errors, whereas the InSAR DSM was characterized by ramps (likely due to orbit shift) and step discontinuities whose values were equal to or multiples of the altitude ambiguity. The errors observed in interferometric and radargrammetric DSMs may represent obstacles for correct hydrological and hydrogeological risk analyses. Nevertheless, since these errors are different based on type and location, the two techniques may complement one another in the sense that the best DSM should be obtained by fusing InSAR and radargrammetric techniques by just using areas where they perform better. Future works should explore both the interferometric unwrapping algorithm improvement to better solving phase ambiguity and the refinement of radargrammetric algorithm sensitivity in order to match a greater number of points, having as a final goal the integration of both potential techniques. Overall, the radargrammetric derived DEMs actually are comparable (in terms of accuracy) to InSAR DEMs, and

in the future when more high-resolution SAR systems will become available, the accuracy of the radargrammetric DEMs will be improved.

Acknowledgements

COSMO-SkyMed images were made available by e-Geos S.p.A., Rome (Italy), under the framework of a collaboration agreement. We are indebted to e-Geos S.p.A. for their generosity. We also thank Dr K. Jacobsen for making the DEMANAL software available, and sarmap SA (Purasca, Switzerland) for the SARscape software and their support during interferometric processing.

References

Capaldo P, Crespi M, Fratarcangeli F, Nascetti A, Pieralice F. 2011. High-resolution SAR radargrammetry: a first application with COSMO-SkyMed SpotLight imagery. IEEE Geosci Remote Sens Lett. 8:1100–1104.

Capaldo P, Crespi M, Fratarcangeli F, Nascetti A, Pieralice F. 2012. A radargrammetric orientation model and a RPCs generation tool for COSMO-SkyMed and TerraSAR-X high resolution SAR. Italian J Remote Sens/Rivista Italiana di Telerilevamento. 44:55–67.

Costantini M. 1998. A novel phase unwrapping method based on network programming. IEEE Trans Geosci Remote Sens. 36:813–821.

Crespi M, Capaldo P, Fratarcangeli F, Nascetti A, Pieralice F. 2010. DSM generation from very high optical and radar sensors: problems and potentialities along the road from the 3D geometric modeling to the surface model. Proceedings of the International Geoscience and Remote Sensing Symposium (IGARSS); 2010 Jul 25–30; New York (NY): IEEE.

Fell R, Corominas J, Bonnard C, Cascini L, Leroi E, Savage WZ. 2008. Guidelines for landslide susceptibility, hazard and risk zoning for land use planning. Eng Geol. 102:85–98.

Ferretti A, Guarnieri AM, Prati C, Rocca F, Massonnet D. 2007. InSAR principles: Guidelines for SAR interferometry, processing and interpretation. Paris: European Space Agency.

Gelautz M, Paillou P, Chen C, Zebker H. 2003. Radar stereo- and interferometry-derived digital elevation models: comparison and combination using Radarsat and ERS-2 imagery. Int J Remote Sens. 24:5243–5264.

Goodman J. 1976. Some fundamental properties of speckle. J Opt Soc Am. 66:1145–1150.

Hanssen RF. 2001. Radar interferometry: data interpolation and error analysis. Dordrecht: Kluwer Academic Publishers.

Heipke C. 1996. Overview of image matching techniques. In: Kölbl O, editor. Proceedings of the OEEPE – Workshop on Application of Digital Photogrammetric Workstations; 1999 Jun 22–24; Marne la Valée.

Ma Y, Soatto S, Kosecka J, Sastry SS. 2004. An invitation to 3D Vision: from images to geometric models. New York (NY): Springer.

Mansourpour M, Rajabi M, Blais J. 2000. Effects and performance of speckle noise reduction filters on active radar and SAR images. Ankara: The Scientific and Technological Research Council of Turkey.

Mason DC, Schumann GJ, Bates PD. 2011. Data utilization in flood inundation modelling. In: Pender G, Faulkner H, editors. Flood risk science and management. New York (NY): Wiley; p. 211–233.

Méric S, Fayard F, Pottier E. 2009. Radargrammetric SAR image processing. In: Ho P-GP, editor. Geoscience and remote sensing. Rijeka: Intech; p. 421–454.

Nascetti A. 2013. High resolution radargrammetry: development and implementation of an innovative image matching strategy [PhD thesis]. Rome: University of Rome "La Sapienza", Faculty of Engineering.

Neal J, Schumann GBates P., 2012. A subgrid channel model for simulating river hydraulics and floodplain inundation over large and data sparse areas. Water Resour Res. 48:1–16.

Park N, Chi K. 2008. Quantitative assessment of landslide susceptibility using high-resolution remote sensing data and a generalized additive model. Int J Remote Sens. 29:247–264.

Perko R, Raggam H, Deutscher J, Gutjahr K, Schardt M. 2011. Forest assessment using high resolution SAR data in X-Band. Remote Sens. 3:792–815.

Sansosti E. 2004. A simple and exact solution for the interferometric and stereo SAR geolocation problem. IEEE Trans Geosci Remote Sens. 42:1625–1634.

Schubert A, Small D, Jehle M, Meier E. 2012. COSMO-SkyMed, TerraSAR-X, and RADARSAT-2 geolocation accuracy after compensation for earth-system effects. Proceedings of the IEEE International Geoscience and Remote Sensing Symposium (IGARSS); 2012 July 22–27; New York (NY): IEEE.

Schumann G, Di Baldassarre G, Alsdorf D, Bates PD. 2010. Near real-time flood wave approximation on large rivers from space: application to the River Po, Italy. Water Resour Res. 46:1–8.

Seymour M, Cumming IG. 1994. Maximum likelihood estimation for SAR interferometry. Proceedings of the International Geoscience and Remote Sensing Symposium; 1994 August 8–12; Pasadena (CA).

Toutin T, Chenier R. 2009. 3-D radargrammetric modeling of RADARSAT-2 ultrafine mode: preliminary results of the geometric calibration. IEEE Geosci Remote Sens Lett. 6:611–615.

van Westen CJ, Castellanos E, Kuriakose SL. 2008. Spatial data for landslide susceptibility, hazard, and vulnerability assessment: an overview. Eng Geol. 102:112–131.

Yamazaki D, Kanae S, Kim H, Oki T. 2011. A physically based description of floodplain inundation dynamics in a global river routing model. Water Resour Res. 47:W0450.

Yang C, Kao S, Lee F, Hung P. 2004. Twelve different interpolation methods: a case study of SURFER 8.0. In: Altan Orhan, editor, Proceedings of the XXth ISPRS Congress Technical Commission II; 2004 July 12–23; Istanbul, Turkey.